



Liang, Y., Zhao, O., Long, Y.-L. and Gardner, L. (2019) Stainless steel channel sections under combined compression and minor axis bending – part 1: experimental study and numerical modelling. *Journal of Constructional Steel Research*, 152, pp. 154-161.

There may be differences between this version and the published version. You are advised to consult the publisher's version if you wish to cite from it.

<http://eprints.gla.ac.uk/186396/>

Deposited on: 10 May 2019

Enlighten – Research publications by members of the University of Glasgow\_  
<http://eprints.gla.ac.uk>

## **Stainless steel channel sections under combined compression and minor axis bending – Part 1: Experimental study and numerical modelling**

Yating Liang <sup>a</sup>, Ou Zhao <sup>\*b</sup>, Yue-ling Long <sup>c</sup>, Leroy Gardner <sup>d</sup>

<sup>a, b</sup> School of Civil and Environmental Engineering, Nanyang Technological University, 50 Nanyang Avenue, 639798 Singapore, Singapore

<sup>c</sup> School of Civil and Transportation Engineering, Guangdong University of Technology, China

<sup>d</sup> Department of Civil and Environmental Engineering, Imperial College London, London, UK

\* Corresponding author, Phone: +65 6790 6934

Email: ou.zhao@ntu.edu.sg

**Abstract:** The local cross-section behaviour of stainless steel channel sections under the combined actions of axial compression and minor axis bending moment is investigated in the present paper and its companion paper, based on a comprehensive experimental and numerical study. Two channel section sizes were considered in the experimental programme, with the test specimens laser-welded at the two flange-to-web junctions from hot-rolled EN 1.4307 and EN 1.4404 austenitic stainless steel plates. The experiments involved initial local geometric imperfection measurements and 15 eccentrically loaded stub column (combined loading) tests. The loading eccentricity was varied to achieve a range of ratios of axial compression to minor axis bending moment; both orientations of bending (web in compression and web in tension) were considered. The test setup and procedures, together with the key experimental observations, including the load-carrying and deformation capacities, load-end rotation histories and failure modes, are fully reported. A finite element simulation study is then presented, in which the models were first validated against the

obtained test results and then employed, in the companion paper, for parametric investigations and the assessment of design provisions.

**Keywords:** Channel sections; Combined loading; Experiments; Finite element modelling; Laser-welded; Stainless steel

## **1. Introduction**

Growing emphasis is being placed on the use of sustainable construction materials in civil and offshore engineering. Stainless steel has excellent corrosion resistance and durability, thus leading to low maintenance and inspection costs during the service life of a structure, and is 100% recyclable with minimal or no degradation in physical and mechanical properties with time. It is therefore gaining increasing viability and traction in terms of material selection for a range of applications. Extensive experimental and numerical studies have been carried out previously, aimed at verifying the structural performance of different types of stainless steel components and devising efficient design approaches. The present study focuses on the cross-section behaviour and design of stainless steel channel sections subjected to combined compression and bending moment. A brief summary of the previous relevant studies is first provided: Kuwamura [1] carried out stub column tests on austenitic stainless steel channel sections to study their load-carrying capacities under pure compression. Theofanous et al. [2] conducted laterally restrained 3-point and 4-point bending tests to investigate the flexural performance of austenitic stainless steel channel sections subjected to both a moment gradient and uniform bending moment, respectively, while Niu et al. [3] performed tests on laterally unrestrained channel section beams to study their overall buckling behaviour. Tests on ferritic stainless steel lipped channel section columns were

carried out by Lecce and Rasmussen [4], Rossi et al. [5] and Becque and Rasmussen [6], in order to investigate their distortional buckling behaviour, interaction of distortional and overall buckling behaviour and interaction of local and overall buckling behaviour, respectively. Although a number of studies have been conducted on stainless steel channel section members subjected to pure compression and pure bending (i.e. isolated loading), there have been no investigations into their structural performance under combined loading.

The present paper and its companion paper [7] describe a comprehensive experimental and numerical study of the local behaviour of stainless steel channel sections subjected to the combined actions of axial compression and minor axis bending moment. A testing programme, including initial local geometric imperfection measurements and 15 eccentrically loaded stub column (combined loading) tests, is firstly described. Following this, a finite element modelling validation study, in which the full load–deformation responses and failure modes of the tested specimens were replicated, is presented. Upon validation of the numerical models against the test results, parametric studies were conducted to generate further structural performance data and are reported in the companion paper. The obtained test data, together with the derived numerical results, are then analysed and employed to assess the accuracy of the current design provisions in the European code EN 1993-1-4 [8] and AISC design guide 27 [9]. Finally, improved design rules are proposed through extension of the continuous strength method (CSM) to the case of stainless steel channel sections under combined loading, and the applicability and reliability of the new design proposals are evaluated.

## 2. Testing programme

### 2.1 General

A testing programme was firstly carried out, aimed at studying the local behaviour and ultimate strength of stainless steel channel sections subjected to combined compression and minor axis bending moment. Two channel section sizes were employed in the testing programme: C 40×40×5×5 and C 100×50×6×9; the cross-section designation system begins with a letter 'C' (indicating a channel section), followed by the nominal section size in millimetres (web width  $h$  × flange width  $b_f$  × web thickness  $t_w$  × flange thickness  $t_f$  - see Fig. 1). The two tested channel sections were fabricated by laser-welding at the two flange-to-web junctions, from hot-rolled EN 1.4307 and EN 1.4404 austenitic stainless steel plates. Overall, the testing programme included imperfection measurements to determine the initial local geometric imperfections of the specimens and 15 eccentrically loaded stub column tests to derive the structural performance of stainless steel channel sections under combined loading.

### 2.2 Material tensile coupon tests

Material tensile coupon tests on the two studied channel sections were carried out by Theofanous et al. [2]; a summary of the testing procedure and results are presented herein. For each cross-section size, four longitudinal coupons were extracted from the middle part of the web and the flanges (see Fig. 1), and then tested using an INSTRON 250 kN testing machine. Displacement control was used in the material tensile coupon tests, with the applied strain rates conforming to the requirements of EN ISO 6892-1 [10]. The average measured material properties for each channel section size are reported in Table 1, in which  $t_n$  is the

nominal thickness of each constituent plate element of the channel section,  $E$  is the Young's modulus,  $\sigma_{0.2}$  is the 0.2% proof stress,  $\sigma_{1.0}$  is the 1.0% proof stress,  $\sigma_u$  is the ultimate tensile stress,  $\varepsilon_u$  is the strain at the ultimate tensile stress,  $\varepsilon_f$  is the plastic strain at fracture measured over the standard gauge length, and  $n$  and  $n'_{0.2,1.0}$  are the exponents used in the two-stage Ramberg–Osgood (R–O) material model [11–14]. Note that channel section C 100×50×6×9 was made up of dissimilar plates, and the corresponding coupon test results are labelled with 'W' and 'F' for web and flange, respectively.

### ***2.3 Residual stresses***

Gardner et al. [15] conducted residual stress measurements on laser-welded stainless steel I-sections, and proposed a representative residual stress pattern; note that corrected values for distribution parameters  $c$  and  $d$  (with  $c=0.0375h_w$  and  $d=0.1h_w$ , where  $h_w$  is the clear distance between the flanges) were presented in [16]. An adaptation of this for channel sections is presented in Fig. 2 [17], where  $a$ ,  $b$ ,  $c$  and  $d$  are the distribution parameters with the values reported in Table 2,  $\sigma_{ft}$  and  $\sigma_{wt}$  are the peak tensile residual stresses in the flange and web, equal to half of the material 0.2% proof stresses of the corresponding plate elements, and  $\sigma_{fc}$  and  $\sigma_{wc}$  are the peak compressive residual stresses in the flange and web, determined on the basis of each constituent plate being in self-equilibrium.

### ***2.4 Initial local geometric imperfection measurements***

Initial local geometric imperfections were measured over a representative 600 mm length of each studied channel section size, using an experimental setup similar to that described in Schafer and Peköz [18]. Measurements were taken along seven longitudinal lines for each

channel section: for the outstand flanges, measurements were taken along the supported edge and the free edge (i.e. the flange tip), while for the web, measurements were conducted along the two supported edges and the centreline. The maximum imperfection amplitude for each constituent plate element was defined as the maximum deviation from a linear trend surface fitted to the corresponding data set [19–22], as reported in Table 3, where  $\omega_{f1}$  and  $\omega_{f2}$  and  $\omega_w$  are the maximum measured local imperfection amplitudes of the two outstand flanges and the web, respectively, while the maximum imperfection amplitude of the specimen  $\omega_0$  was taken as the largest measured deviation from all three constituent plates of the channel section.

### ***2.5 Eccentrically loaded stub column (combined loading) tests***

For each of the two studied channel sections, five eccentrically loaded stub column tests were conducted about the minor axis in the ‘n’ orientation, inducing the maximum compressive stress in the web. In addition to the ten ‘n’ orientation combined loading tests, five further tests were also carried out on the C 100×50×6×9 specimens in the ‘u’ orientation, which induced the maximum tensile (or the minimum compressive, in some cases) stress in the web of the channel section. The initial loading eccentricity, defined as the distance from the loading point to the cross-section elastic neutral axis, was designed to vary between 10 mm and 40 mm, which resulted in a range of proportions of bending moment-to-axial load being considered. The nominal length of each eccentrically loaded stub column specimen was chosen in accordance with the guidelines of Ziemian [23] to be short enough to prevent any significant influence from global instability but still long enough to incorporate a representative pattern of residual stresses and initial local geometric imperfections. The measured length and geometric dimensions of each specimen are reported in Table 4, where  $L$  is the member length,  $h$  and  $b_f$  are the outer web width and flange width of the channel

section, respectively, and  $t_w$  and  $t_f$  are the web thickness and flange thickness, respectively. For each eccentrically loaded channel section stub column, the distances of the elastic and plastic neutral axes (ENA and PNA) from the outer face of the web, denoted  $y_e$  and  $y_p$ , respectively, have been calculated and also provided in Table 4. The adopted specimen ID system comprises a number and a letter (e.g., 2B); the number identifies the section size and bending orientation, with '1' for the C 40×40×5×5 section under combined compression and minor axis bending moment in the 'n' orientation, and '2' and '3' for the C 100×50×6×9 section under combined compression and minor axis bending in the 'n' and 'u' orientations, respectively, while the letters A–E designate the varying eccentricities used in each test series.

The eccentrically loaded stub column tests were carried out using an INSTRON 500 kN hydraulic testing machine with knife-edges at both ends to provide pin-ended boundary conditions about the axis of buckling, as shown in Fig. 3; note that the distance from each end of the specimen to the tip of the knife-edge is equal to 87 mm. Displacement control was adopted to drive the test machine at a constant speed of 0.2 mm/min. The test setup is similar to that used by Torabian et al. [24] for conducting beam-column tests on cold-formed carbon steel lipped channel sections, as depicted in Fig. 3, consisting of one LVDT, positioned at the mid-height of the specimen along the buckling direction to record the lateral deflection, two inclinometers, located at both member ends to measure the end rotation, and two pairs of strain gauges, affixed to the flange tips and outer face of the web at the mid-height of the specimen, to capture the maximum and minimum longitudinal strains. The strain gauge readings were utilised together with the measured lateral deflection from the LVDT [20–22,25,26], to calculate the actual initial loading eccentricities of the channel section specimens subjected to combined minor axis bending moment and compression, with the derivation procedures described as follows.

During the early stage of loading (e.g., less than 10% of the predicted ultimate load), the structural response is essentially linear elastic, and the initial neutral axis position is located at the elastic neutral axis. In the combined loading tests, the longitudinal strains comprise two components: (i) strains due to the applied axial compressive load  $\varepsilon_c$ , and (ii) strains due to the bending moment  $\varepsilon_b$ , with  $\varepsilon_{b,c}$  and  $\varepsilon_{b,t}$  denoting the outer-fibre compressive and tensile strains due to bending, respectively, as illustrated in Fig. 4. Therefore, the maximum compressive strains  $\varepsilon_{max}$  are equal to the sum of  $\varepsilon_c$  and  $\varepsilon_{b,c}$ , while the measured maximum tensile (or the minimum compressive, in some cases) strains  $\varepsilon_{min}$  are equal to the difference between  $\varepsilon_c$  and  $\varepsilon_{b,t}$ , as given by Eqs (1) and (2), respectively.

$$\varepsilon_c + \varepsilon_{b,c} = \varepsilon_{max} \quad (1)$$

$$\varepsilon_c - \varepsilon_{b,t} = \varepsilon_{min} \quad (2)$$

For channel sections bent about the minor axis in the ‘n’ orientation, as shown in Fig. 4(a), the relationship between  $\varepsilon_{b,c}$  and  $\varepsilon_{b,t}$  is defined by Eq. (3), and the values of the corresponding bending strains ( $\varepsilon_{b,c}$  and  $\varepsilon_{b,t}$ ) can be determined by solving Eqs (1)–(3) simultaneously, as given by Eqs (4) and (5).

$$\varepsilon_{b,t} = \frac{b_f - y_e}{y_e} \varepsilon_{b,c} \quad (3)$$

$$\varepsilon_{b,c} = \frac{\varepsilon_{max} - \varepsilon_{min}}{1 + (b_f - y_e)/y_e} \quad (4)$$

$$\varepsilon_{b,t} = \frac{\varepsilon_{max} - \varepsilon_{min}}{1 + (b_f - y_e)/y_e} \frac{b_f - y_e}{y_e} \quad (5)$$

For channel sections under combined compression and bending moment in the ‘u’ orientation (see Fig. 4(b)), upon identification of the relationship between  $\varepsilon_{b,c}$  and  $\varepsilon_{b,t}$ , as given by Eq. (6), their values can be calculated from Eqs (7) and (8), respectively.

$$\varepsilon_{b,t} = \frac{y_e}{b_f - y_e} \varepsilon_{b,c} \quad (6)$$

$$\varepsilon_{b,c} = \frac{\varepsilon_{max} - \varepsilon_{min}}{1 + y_e / (b_f - y_e)} \quad (7)$$

$$\varepsilon_{b,t} = \frac{\varepsilon_{max} - \varepsilon_{min}}{1 + y_e / (b_f - y_e)} \frac{y_e}{b_f - y_e} \quad (8)$$

The bending moment at the mid-height of the specimen can then be derived from  $M=EI_z\kappa$ , where  $I_z$  is the second moment of area about the minor axis and  $\kappa=(\varepsilon_{b,c}+\varepsilon_{b,t})/b_f$  is the curvature. The mid-height bending moment can also be calculated from  $M=N(e_{0e}+\Delta)$ , in which  $N$  is the applied compressive load,  $e_{0e}$  is the initial loading eccentricity (i.e. the distance from the loading point to the cross-section elastic neutral axis) and  $\Delta$  is the mid-height lateral deflection measured from the LVDT. By equating the two (i.e.  $EI_z\kappa=N(e_{0e}+\Delta)$ ), the final expression for  $e_{0e}$  can be derived, as given by Eq. (9).

$$e_{0e} = \frac{EI_z (\varepsilon_{max} - \varepsilon_{min})}{b_f N} - \Delta \quad (9)$$

The key experimental results for each eccentrically loaded stub column specimen are summarised in Table 5, where  $e_{0e}$  is the initial loading eccentricity from the elastic neutral axis, calculated from Eq. (9),  $e_{0p}$  is the corresponding initial loading eccentricity from the plastic neutral axis, which is equal to  $e_{0e}-(y_e-y_p)$  and  $e_{0e}+(y_e-y_p)$  for the minor axis combined loading tests in the ‘n’ and ‘u’ orientations, respectively,  $N_u$  is the failure load,  $e'$  and  $\phi_u$  are the mid-height lateral deflection and end rotation at the failure load, respectively, and

$M_{ue}=N_u(e_{0e}+e')$  and  $M_{up}=N_u(e_{0p}+e')$  are the failure bending moments, calculated based on the assumption that the neutral axis positions at failure are located at the elastic and plastic neutral axes, respectively. The experimental load–end rotation curves for the two series of minor axis combined loading tests conducted in the ‘n’ orientation are depicted in Figs 5(a) and 5(b), while the experimental load–end rotation histories for the C 100×50×6×9 specimens under combined axial force and minor axis bending moment in the ‘u’ orientation are shown in Fig. 6. Typical local buckling failure modes of specimens C 100×50×6×9-2E and C 100×50×6×9-3B subjected to combined compression and minor axis bending moment in the ‘n’ and ‘u’ orientations are displayed in Figs 7 and 8, respectively.

### **3. Numerical modelling**

#### ***3.1 Basic numerical modelling assumptions***

In conjunction with the experimental investigation, a numerical simulation programme was carried out by means of the general-purpose finite element analysis software ABAQUS [27]. The numerical models were initially validated against the experimental results reported in Section 2 and then utilised to conduct parametric studies to extend the test data pool over a broader range of cross-section proportions and loading combinations in the companion paper [7].

The four-noded doubly curved shell element allowing finite membrane strains and large rotations, S4R [27] has been successfully utilised by the authors in previous numerical simulations of stainless steel thin-walled structural members subjected to combined loading [20,22,28–31], and was thus also employed herein. With regards to the mesh size, the

longitudinal element length was set equal to the minimum of the measured flange and web thicknesses of the channel section  $t_m$ ; this mesh size was found to offer a suitable balance between accuracy and computational efficiency, following a sensitivity study considering a range of element sizes from  $0.5t_m$  to  $3t_m$ . The element widths along the cross-section centreline depended on the widths of the strips in the applied residual stress distribution pattern, as shown in Fig. 2. Specifically, an element width equal to the minimum of the measured flange and web thicknesses was adopted in the constant peak tensile and compressive residual stress regions of the modelled channel section, while a finer mesh of three elements was assigned to the transition regions [17]; this ensured an accurate representation of the residual stress pattern in the FE models. Fig. 9 depicts a typical residual stress distribution used in the FE models for the C 100×50×6×9 specimens. The measured engineering material stress–strain responses were firstly represented by the two-stage Ramberg–Osgood material model [11–14], and then converted into the format of true stress and log plastic strain, before inputting into ABAQUS. The stress–strain curves exhibited the characteristic rounded behavior with significant strain hardening associated with stainless steel.

Regarding the modelling of boundary conditions, the end sections of each combined loading FE model were coupled to two eccentric reference points, with the eccentricities equal to the corresponding values employed in the tests. The reference point at the loaded end was set free to rotate about the minor axis and translate in the longitudinal direction, while the other reference point was only allowed to rotate about the minor axis, in order to simulate the pin-ended boundary conditions provided by the knife-edges in the eccentrically loaded stub column tests. Moreover, the eccentric reference points were offset longitudinally from the

end sections by 87 mm, which is equal to the distance from the end of the specimen to the tip of the knife-edge in the tests.

The effect of the initial local geometric imperfection on the local buckling behaviour of stainless steel channel sections subjected to combined compression and bending moment was considered in the numerical modelling. The initial local imperfection pattern along the model length was taken as the lowest elastic local buckling mode shape under the applied combined loading condition, determined through an elastic eigenvalue buckling analysis [17,22,28,30]. Three local imperfection amplitudes were utilised to factor the derived imperfection distribution, in order to study the sensitivity of the numerical models to various imperfection levels and to seek the most suitable imperfection amplitudes to be employed in the parametric studies. The three considered imperfection amplitudes were (1) the maximum measured initial local geometric imperfection amplitude  $\omega_0$ , (2) 1/100 of the maximum of the flange and web thicknesses of the channel section and (3) the imperfection amplitude determined from the modified Dawson and Walker (D&W) model  $\omega_{D\&W}$  [32,33], as given by Eq. (10), in which  $\sigma_{cr,min}$  is the elastic buckling stress of the most slender plate element of the channel section and  $t$  is the thickness of the plate element. Upon incorporation of the initial local geometric imperfections into the FE models, geometrically and materially nonlinear analyses (GMNIA) were carried out to simulate the full load–deformation histories of the tested stainless steel channel section specimens under combined compression and minor axis bending moment; the modified Riks method [34] was the adopted numerical solution technique, which is well suited for the determination of the nonlinear static load–deformation response of structures prone to instability, including the post-ultimate path [35].

$$\omega_{D\&W} = 0.023 \left( \frac{\sigma_{0.2}}{\sigma_{cr,min}} \right) t \quad (10)$$

### ***3.2 Validation of the numerical models***

The accuracy of the finite element models was assessed by comparing the numerically derived ultimate loads, full load-deformation curves and failure modes with those obtained from the experiments. Table 6 shows the ratios of the numerical failure loads to the experimental failure loads for the three considered imperfection levels, revealing that all three generally lead to accurate and consistent failure load predictions, while the best agreement between the test and numerical results was obtained when the imperfection amplitudes predicted by the modified Dawson and Walker model [32,33] were utilised in the developed numerical models.

Comparisons between the test and numerical load–end rotation curves for typical channel section specimens subjected to combined compression and bending moment in the ‘n’ and ‘u’ orientations are shown in Figs 10 and 11, revealing that the full experimental load–deformation histories, including the post-ultimate responses, are accurately replicated by the finite element simulations. The numerical load–end rotation curves derived from FE simulations without the inclusion of residual stresses are also plotted in Figs 10 and 11; the results with and without residual stresses may be seen to almost coincide, indicating that residual stresses have a minimal influence on the local buckling behaviour of stainless steel channel sections subjected to combined loading. The local buckling failure modes derived from numerical modelling are also in good agreement with those obtained from the experiments, as shown in Figs 7 and 8.

Overall, the developed numerical models have been shown to be capable of replicating the full experimental responses and failure modes of the eccentrically loaded stainless steel channel section stub columns, and are therefore considered to be suitable for the generation

of parametric results. Parametric studies and the assessment and development of design provisions are presented in the companion paper [7].

#### **4. Conclusions**

An experimental study into the local cross-section behaviour of laser-welded stainless steel channel sections under combined axial compressive load and minor axis bending moment has been performed and reported in this paper. Overall, the experimental programme included material testing, initial local geometric imperfection measurements, and 15 combined loading tests, conducted with various initial loading eccentricities and in both the ‘n’ and ‘u’ orientations. The experimental setup and procedures for the combined loading tests, together with the key derived experimental results, including the ultimate loads, load–end rotation curves and local buckling failure modes, were fully reported. The test results were then employed in a parallel numerical study for the validation of the finite element models. The developed numerical models were shown to be capable of replicating the full experimental load–deformation responses and failure modes of the eccentrically loaded stainless steel channel section stub column specimens, and are thus considered to be suitable for conducting parametric studies, which are presented in the companion paper [7]. Both the derived test data and numerical results are utilised in the companion paper [7] to evaluate the accuracy of the current codified design rules for stainless steel channel sections subjected to combined compression and minor axis bending moment, and to develop more efficient design approaches.

## **Acknowledgements**

The authors would like to thank Mr. Gordon Herbert from Imperial College London for his assistance in the experimental program.

## **References**

- [1] Kuwamura H. Local buckling of thin-walled stainless steel members. *International Journal of Steel Structures*, 2003;3(3):191–201.
  
- [2] Theofanous M, Liew A, Gardner L. Experimental study of stainless steel angles and channels in bending. *Structures*, 2015;4:80–90.
  
- [3] Niu S, Rasmussen KJR, Fan F. Distortional–global interaction buckling of stainless steel C-beams: Part I - Experimental investigation. *Journal of Constructional Steel Research*, 2014;96:127–39.
  
- [4] Lecce M, Rasmussen KJR. Distortional buckling of cold-formed stainless steel sections: experimental investigation. *Journal of Structural Engineering (ASCE)*, 2006;132(4):497–504.
  
- [5] Rossi B, Jaspart JP, Rasmussen KJR. Combined distortional and overall flexural-torsional buckling of cold-formed stainless steel sections: experimental investigations. *Journal of Structural Engineering (ASCE)*, 2010;136(4):361–9.
  
- [6] Becque J, Rasmussen KJR. Experimental investigation of the interaction of local and overall buckling of stainless steel I-columns. *Journal of Structural Engineering (ASCE)*, 2009;135(11):1340–8.

- [7] Liang Y, Zhao O, Long Y, Gardner L. Laser-welded stainless steel channel sections under combined compression and minor axis bending – Part 2: Parametric studies and design. *Journal of Constructional Steel Research*, submitted.
- [8] EN 1993-1-4:2006+A1:2015. Eurocode 3: Design of steel structures – Part 1.4: General rules – Supplementary rules for stainless steels, including amendment A1 (2015). Brussels: European Committee for Standardization (CEN); 2015.
- [9] AISC. Design Guide 27: Structural Stainless Steel. American Institute of Steel Construction (AISC); 2013.
- [10] EN ISO 6892-1. Metallic materials – Tensile testing. Part 1: Method of test at room temperature. Brussels: European Committee for Standardization (CEN); 2009.
- [11] Ramberg W, Osgood WR. Description of stress–strain curves by three parameters. Technical note No 902, Washington DC: National advisory committee for aeronautics. 1943.
- [12] Hill HN. Determination of stress–strain relations from offset yield strength values. Technical note No 927, Washington DC: National advisory committee for aeronautics. 1944.
- [13] Mirambell E, Real E. On the calculation of deflections in structural stainless steel beams: An experimental and numerical investigation. *Journal of Constructional Steel Research*, 2000;54(1):109–33.
- [14] Gardner L, Ashraf M. Structural design for non-linear metallic materials. *Engineering Structures*, 2006;28(6):926–34.

- [15] Gardner L, Bu Y, Theofanous M. Laser-welded stainless steel I-sections: Residual stress measurements and column buckling tests. *Engineering Structures*, 2016;127:536–48.
- [16] Bu Y, Gardner L. Local stability of laser-welded I-sections in bending. *Journal of Constructional Steel Research*, submitted.
- [17] Liang Y, Wang F, Zhao O, Long Y, Gardner L. Cross-section resistance of stainless steel channel sections subjected to combined axial compression and major axis bending. *Journal of Constructional Steel Research*, submitted.
- [18] Schafer BW, Peköz T. Computational modeling of cold-formed steel: characterizing geometric imperfections and residual stresses. *Journal of Constructional Steel Research*, 1998;47(3):193–210.
- [19] Zhao O, Gardner L, Young B. Experimental Study of Ferritic Stainless Steel Tubular Beam-Column Members Subjected to Unequal End Moments. *Journal of Structural Engineering (ASCE)*, 2016; 142(11):04016091.
- [20] Zhao O, Gardner L, Young B. Buckling of ferritic stainless steel members under combined axial compression and bending. *Journal of Constructional Steel Research*, 2016;117:35–48.
- [21] Zhao O, Rossi B, Gardner L, Young, B. Behaviour of structural stainless steel cross-sections under combined loading – Part I: Experimental study. *Engineering Structures*, 2015;89:236–46.

- [22] Zhao O, Rossi B, Gardner L, Young B. Experimental and numerical studies of ferritic stainless steel tubular cross-sections under combined compression and bending. *Journal of Structural Engineering (ASCE)*, 2016;142(2):04015110.
- [23] Ziemian RD. *Guide to stability design criteria for metal structures*, 6<sup>th</sup> Edition. John Wiley & Sons, Inc., New York (USA), 2010.
- [24] Torabian S, Zheng B, Schafer BW. Experimental response of cold-formed steel lipped channel beam-columns. *Thin-Walled Structures*, 2015;89:152–68.
- [25] Huang Y, Young B. Experimental investigation of cold-formed lean duplex stainless steel beam-columns. *Thin-Walled Structures*, 2014;76:105–17.
- [26] Arrayago I, Real E. Experimental study on ferritic stainless steel RHS and SHS cross-sectional resistance under combined loading. *Structures*, 2015;4:69–79.
- [27] Hibbitt, Karlsson & Sorensen, Inc. ABAQUS. ABAQUS/Standard user's manual volumes I-III and ABAQUS CAE manual. Version 6.12. Pawtucket (USA); 2012.
- [28] Zhao O, Gardner L, Young B. Structural performance of stainless steel circular hollow sections under combined axial load and bending – Part 1: Experiments and numerical modelling. *Thin-Walled Structures*, 2016;101:231–9.
- [29] Zhao O, Gardner L, Young B. Testing and numerical modelling of austenitic stainless steel CHS beam-columns. *Engineering Structures*, 2016;111:263–74.

- [30] Zhao O, Rossi B, Gardner L, Young B. Behaviour of structural stainless steel cross-sections under combined loading – Part II: Numerical modelling and design approach. *Engineering Structures*, 2015;89:247–59.
- [31] Zhao O, Gardner L, Young B. Behaviour and design of stainless steel SHS and RHS beam-columns. *Thin-Walled Structures*, 2016;106:330–45.
- [32] Dawson RG, Walker AC. Post-buckling of geometrically imperfect plates. *Journal of the Structural Division (ASCE)*, 1972;98(1):75–94.
- [33] Gardner L, Nethercot DA. Numerical modeling of stainless steel structural components – A consistent approach. *Journal of Structural Engineering (ASCE)*, 2004;130(10):1586–601.
- [34] Riks E. An incremental approach to the solution of snapping and buckling problems. *International Journal of Solids and Structures*, 1979;15(7):529–51.
- [35] Crisfield MA, Remmers JJ, Verhoosel CV. *Nonlinear finite element analysis of solids and structures*. John Wiley & Sons; 2012.

**Table 1** Summary of key measured material properties from the tensile coupon tests.

Cross-section	$t_n$	$E$	$\sigma_{0.2}$	$\sigma_{1.0}$	$\sigma_u$	$\varepsilon_u$	$\varepsilon_f$	R-O exponents	
	(mm)	(GPa)	(MPa)	(MPa)	(MPa)	(%)	(%)	$n$	$n'_{0.2,1.0}$
C 40×40×5×5	5	190	292	383	659	57	69	4.8	3.5
C 100×50×6×9-W	6	185	258	340	576	49	64	3.7	3.3
C 100×50×6×9-F	9	196	275	337	604	51	67	5.8	2.5

**Table 2** Distribution parameters in residual stress model for laser-welded stainless steel channel sections.

Parameter	a	b	c	d
	$0.2b_f$	$0.075b_f + 0.5t_w$	$0.0375h_w$	$0.1h_w$

**Table 3** Measured initial local geometric imperfection amplitudes.

Cross-section	$\omega_{f1}$	$\omega_{f2}$	$\omega_w$	$\omega_0$
	(mm)	(mm)	(mm)	(mm)
C 40×40×5×5	0.48	0.29	0.30	0.48
C 100×50×6×9	0.38	0.21	0.13	0.38

**Table 4** Measured geometric properties for channel section specimens.

Cross-section	Orientation	Specimen ID	$L$ (mm)	$h$ (mm)	$b_f$ (mm)	$t_w$ (mm)	$t_f$ (mm)	$y_e$ (mm)	$y_p$ (mm)
C 40×40×5×5	n	1A	119.5	40.00	40.02	4.63	4.80	15.27	12.68
		1B	120.3	39.98	40.02	4.63	4.80	15.27	12.68
		1C	119.9	40.00	39.95	4.60	4.82	15.27	12.73
		1D	120.2	40.02	39.98	4.60	4.81	15.27	12.72
		1E	120.3	40.00	39.98	4.61	4.82	15.28	12.73
C 100×50×6×9	n	2A	300.0	100.30	49.50	5.95	8.79	16.88	10.75
		2B	299.8	100.30	49.49	5.92	8.80	16.91	10.84
		2C	299.7	100.35	49.51	5.93	8.78	16.89	10.78
		2D	300.1	100.32	49.53	5.94	8.81	16.92	10.83
		2E	300.0	100.31	49.52	5.95	8.80	16.90	10.78
C 100×50×6×9	u	3A	300.1	100.31	49.48	5.92	8.82	16.92	10.87
		3B	300.0	100.32	49.50	5.95	8.80	16.89	10.77
		3C	300.0	100.33	49.51	5.93	8.79	16.90	10.80
		3D	300.1	100.30	49.50	5.94	8.81	16.90	10.81
		3E	300.0	100.34	49.50	5.93	8.82	16.92	10.85

**Table 5** Summary of channel section combined loading test results.

Cross-section	Orientation	Specimen ID	$e_{0e}$ (mm)	$e_{0p}$ (mm)	$N_u$ (kN)	$e'$ (mm)	$\phi_u$ (deg)	$M_{ue}$ (kNm)	$M_{up}$ (kNm)
C 40×40×5×5	n	1A	9.4	6.8	133.2	4.6	1.9	1.9	1.5
		1B	15.4	12.8	103.4	4.2	2.1	2.0	1.8
		1C	21.4	18.9	85.0	5.1	2.5	2.3	2.0
		1D	25.3	22.7	72.0	5.9	2.8	2.2	2.1
		1E	29.4	26.9	65.1	6.7	3.4	2.4	2.2
C 100×50×6×9	n	2A	11.6	5.5	265.0	6.0	1.9	4.7	3.0
		2B	17.8	11.7	216.6	7.9	2.3	5.6	4.3
		2C	21.4	15.3	189.1	7.5	2.5	5.5	4.3
		2D	30.2	24.1	149.0	5.2	2.8	5.3	4.4
		2E	40.2	34.1	119.3	8.8	3.1	5.8	5.1
C 100×50×6×9	u	3A	12.4	18.4	206.0	5.3	1.7	3.6	4.9
		3B	17.1	23.2	169.5	6.2	2.2	3.9	5.0
		3C	19.6	25.7	150.8	7.2	2.4	4.0	5.0
		3D	31.5	37.6	119.5	8.9	3.3	4.8	5.6
		3E <sup>a</sup>	–	–	–	–	–	–	–

<sup>a</sup> Fracture of welds occurred prior to the failure of specimen.

**Table 6** Comparison of test failure loads with FE failure loads for varying imperfection amplitudes.

Cross-section	Orientation	Specimen ID	$e_{0e}$ (mm)	FE $N_u$ /Test $N_u$		
				$\omega_0$	$t/100$	$\omega_{D\&W}$
C 40×40×5×5	n	1A	9.4	0.89	0.90	0.91
		1B	15.4	0.91	0.92	0.92
		1C	21.4	0.92	0.92	0.92
		1D	25.3	0.97	0.97	0.97
		1E	29.4	0.96	0.96	0.96
C 100×50×6×9	n	2A	11.6	0.91	0.92	0.92
		2B	17.8	0.91	0.92	0.92
		2C	21.4	0.94	0.95	0.95
		2D	30.2	0.96	0.96	0.97
		2E	40.2	0.97	0.97	0.97
C 100×50×6×9	u	3A	12.4	0.93	0.92	0.92
		3B	17.1	0.96	0.96	0.96
		3C	19.6	1.01	1.01	1.01
		3D	31.5	0.97	0.97	0.97
		3E <sup>a</sup>	–	–	–	–
Mean			0.94	0.95	0.95	
COV			0.04	0.03	0.03	

<sup>a</sup> Fracture of welds occurred prior to the failure of specimen.

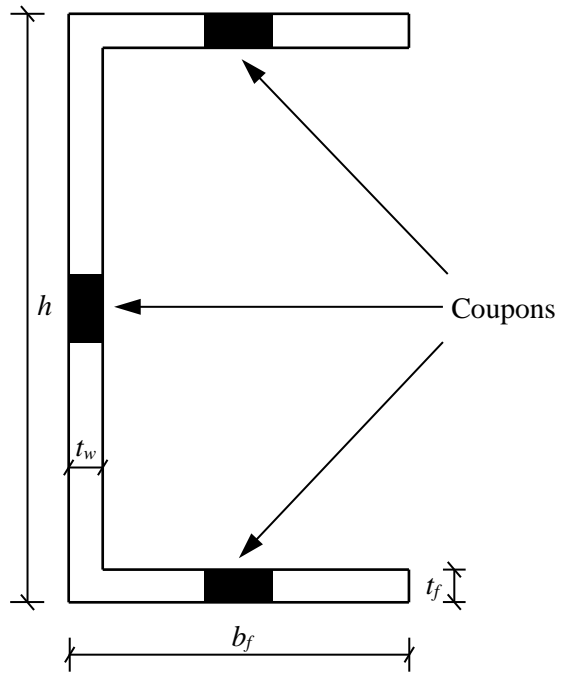


**Fig. 1.** Notation and location from which tensile coupons were extracted from channel sections.

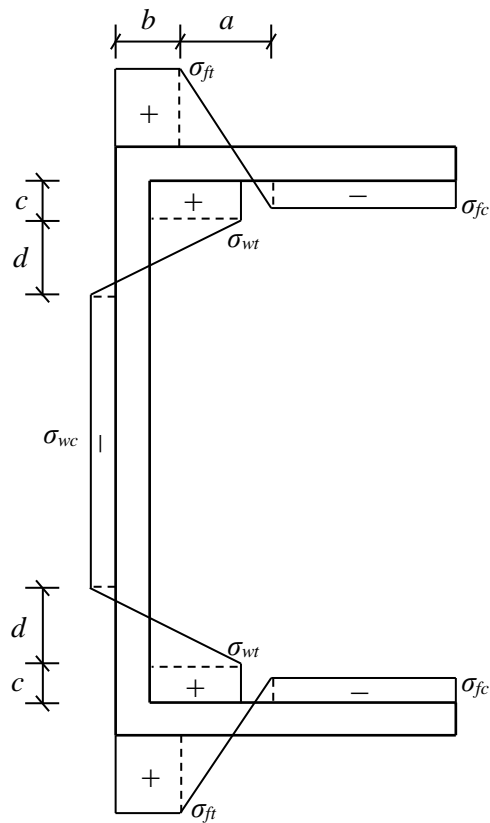
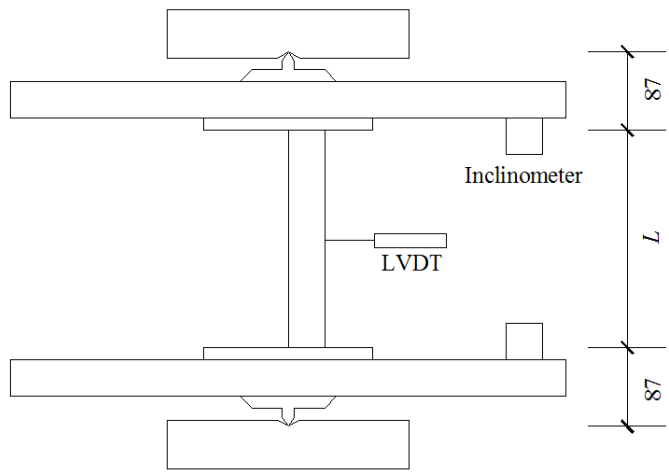


**Fig. 2.** Residual stress pattern for laser-welded stainless steel channel sections [17].

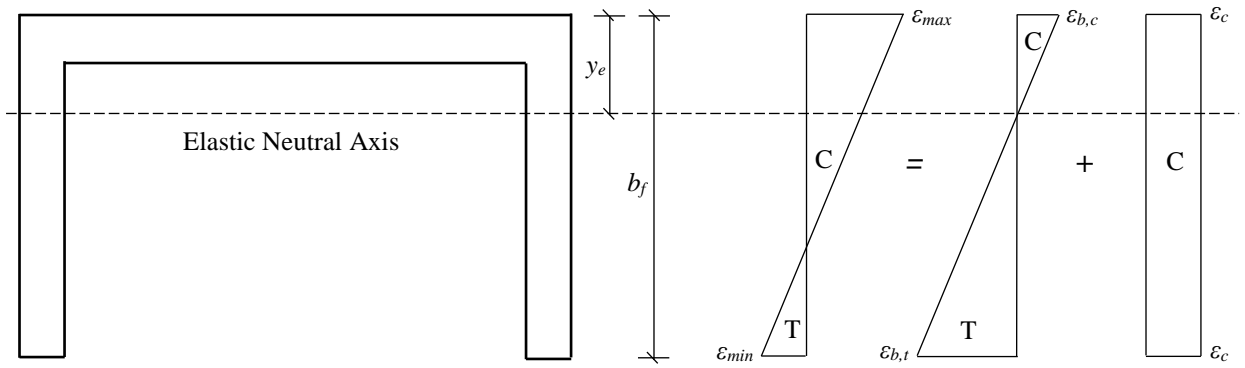


(a) Photograph

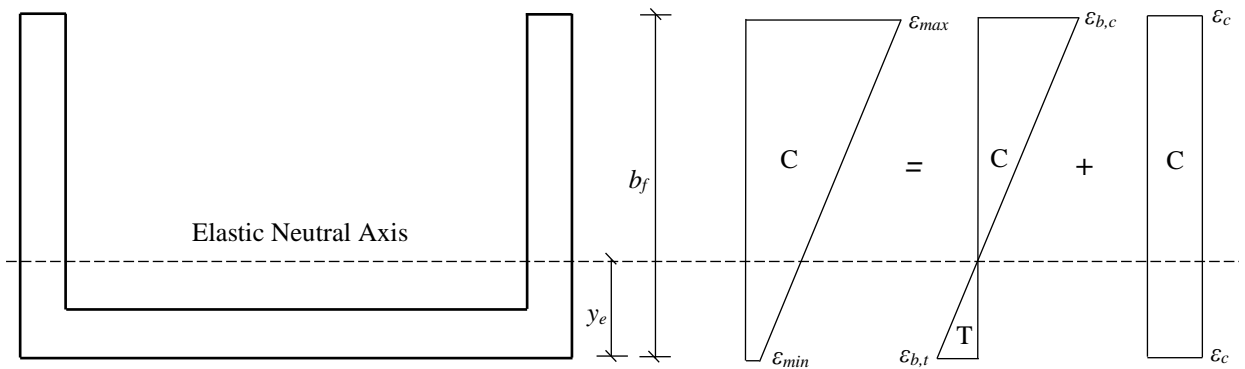


(b) Schematic diagram (dimensions in mm)

**Fig. 3.** Combined loading test setup.

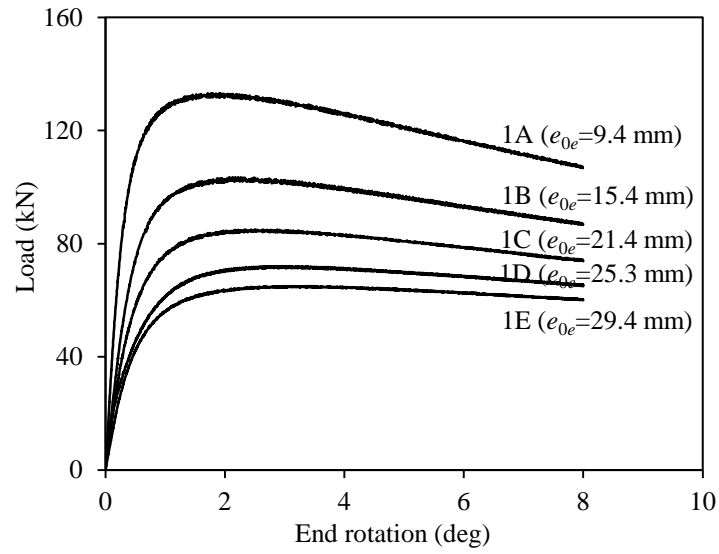


(a) In the 'n' orientation

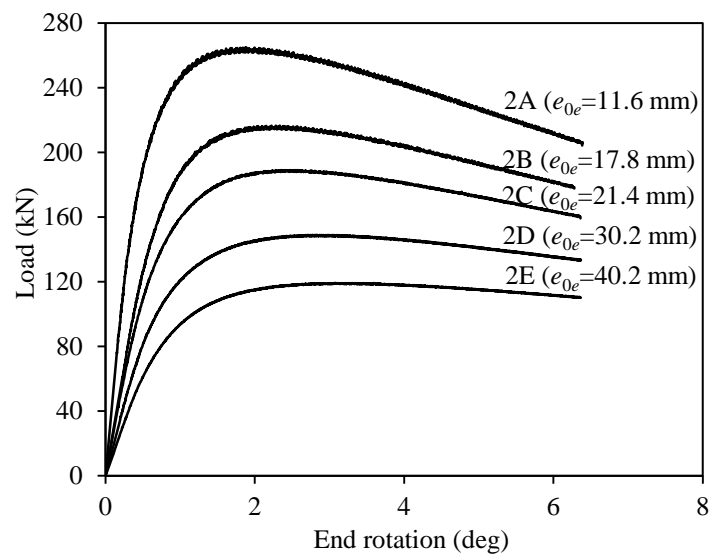


(a) In the 'u' orientation

**Fig. 4.** Illustration of strain distributions for channel sections under combined compression and minor axis bending moment in the 'n' and 'u' orientations, where the maximum compression arises in the web in the 'n' orientation and in the flange tips in the 'u' orientation. Note that 'C' indicates compressive strains, while 'T' identifies tensile strains.



(a) C 40x40x5x5 specimens.



(b) C 100x50x6x9 specimens.

**Fig. 5.** Load–end rotation curves for channel section specimens under combined compression and minor axis bending moment in the ‘n’ orientation.

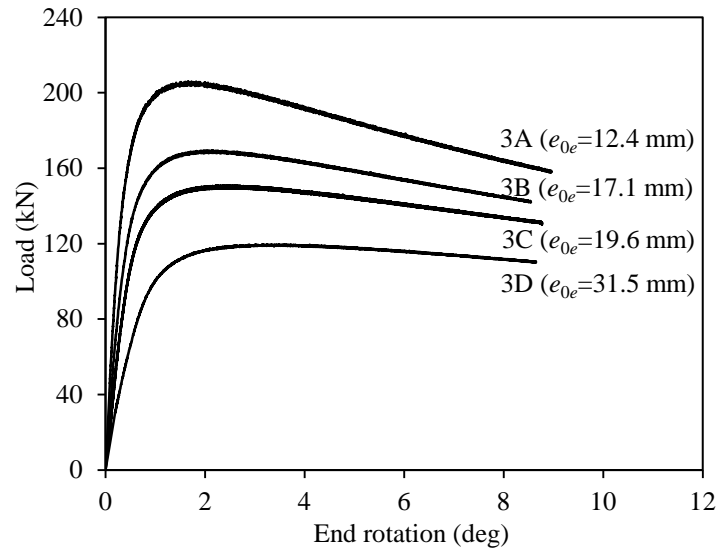


**Fig. 6.** Load–end rotation curves for channel section C 100×50×6×9 specimens under combined compression and minor axis bending moment in the ‘u’ orientation.

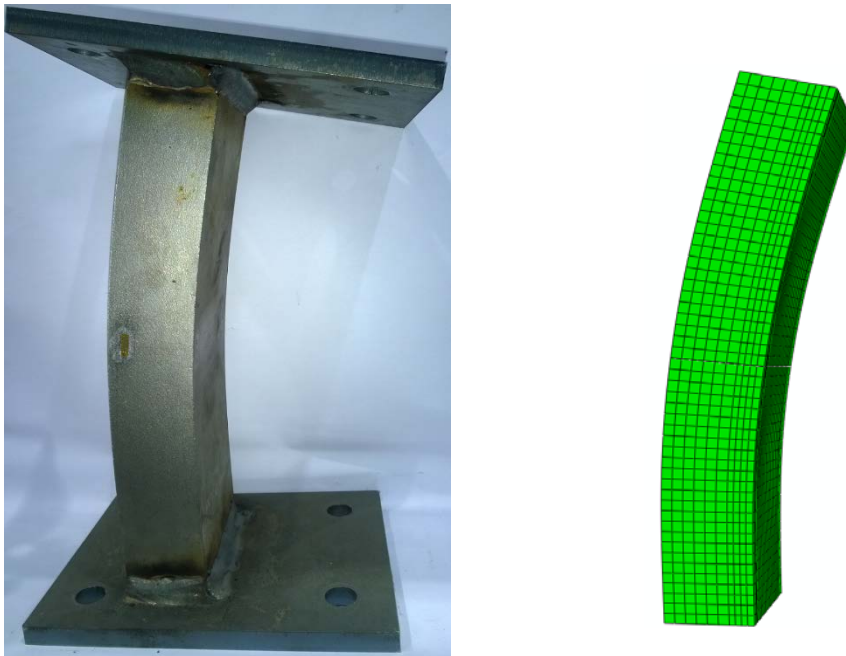


**Fig. 7.** Experimental and numerical failure modes for specimen C 100×50×6×9-2E under combined compression and minor axis bending moment in the ‘n’ orientation.

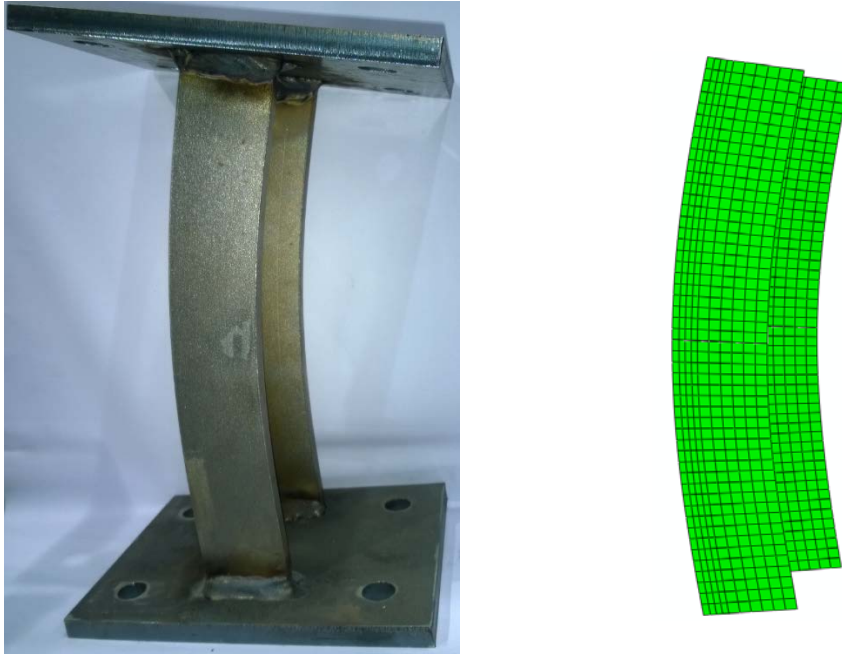


**Fig. 8.** Experimental and numerical failure modes for specimen C 100×50×6×9-3B under combined compression and minor axis bending moment in the ‘u’ orientation.

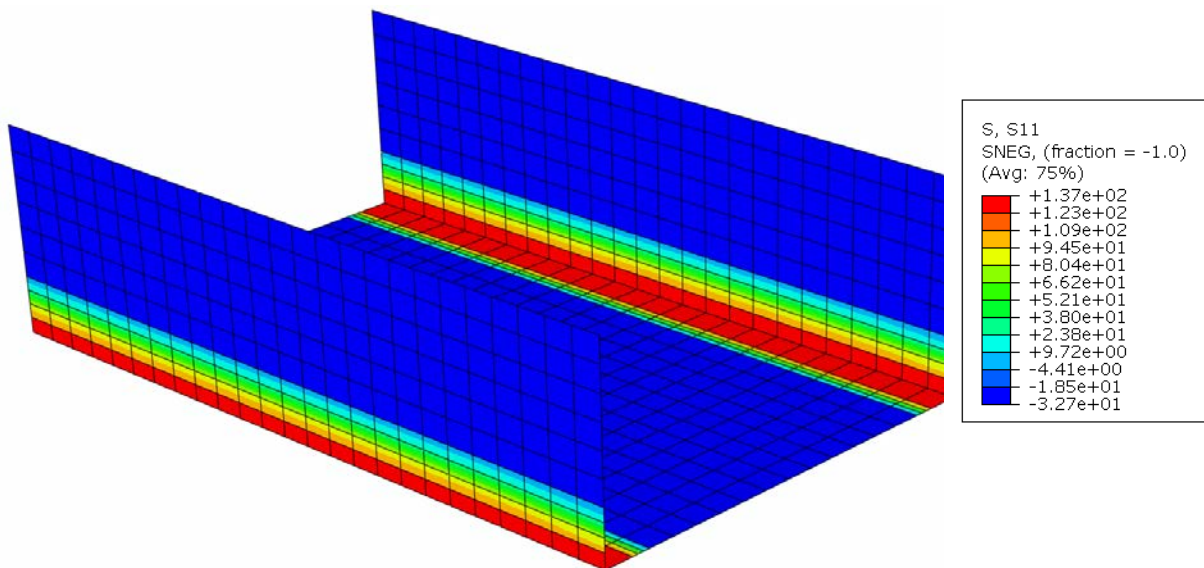


**Fig. 9.** Typical residual stress distribution (in N/mm<sup>2</sup>) in FE models for C 100×50×6×9 specimens. Positive values indicate tensile residual stresses while negative values indicate compressive residual stresses.

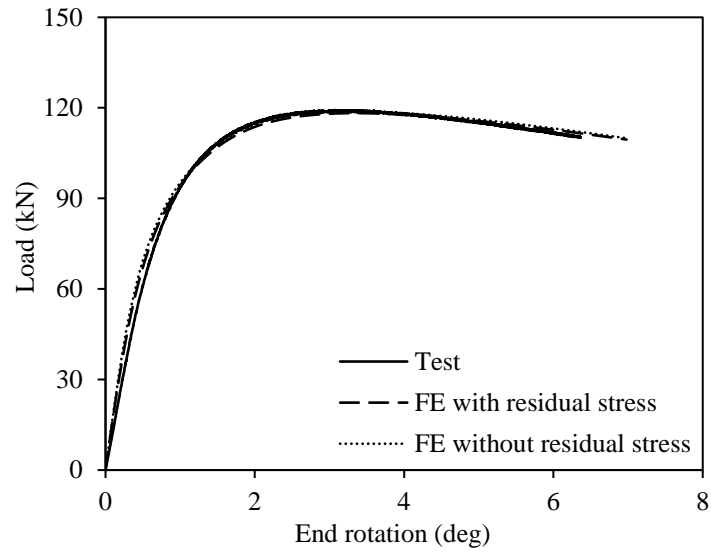


**Fig. 10.** Experimental and numerical load–end rotation curves for specimen C 100×50×6×9-2E under combined compression and minor axis bending moment in the ‘n’ orientation.

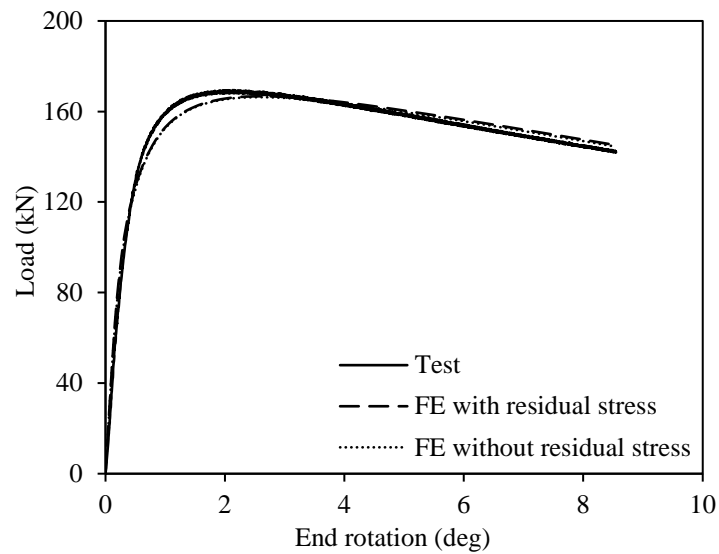


**Fig. 11.** Experimental and numerical load–end rotation curves for specimen C 100×50×6×9-3B under combined compression and minor axis bending moment in the ‘u’ orientation.